Multipurpose imaging-plate camera for in-situ powder XRD at the GILDA beamline

C. Meneghini,[a,b]* G. Artioli,[c] A. Balerna,[d] A. F. Gualtieri,[e] P. Norby [f] and S. Mobilio[b,d]

[a]*Istituto Nazionale di Fisica della Materia (INFM), c/o GILDA-ESRF BP 220, F-38043 Grenoble, France,* [b]*Dip. di Fisica 'E. Amaldi' Universitá di Roma Tre, Via della Vasca Navale 84, I-00146 Roma, Italy,* [c]*Dipartimento di Scienze della Terra, Universitá di Milano, Via Botticelli 23, I-20133 Milano, Italy,* [d]*Laboratori Nazionali di Frascati dell'INFN PO Box 13, I-00044 Frascati, Italy,* [e]*Dipartimento di Scienze della Terra, Universitá di Modena e Reggio Emilia, Via S. Eufemia 19, I-41100 Modena, Italy, and* [f]*Department of Chemistry, University of Oslo, PO BOX 1033, Blindern N-0315 Oslo, Norway. E-mail: meneghini@fis.uniroma3.it*

An Imaging-Plate (IP) camera for X-ray powder diffraction (XRPD) experiments was installed on the synchrotron radiation beamline GILDA at the ESRF. The IP camera can be used in fixed data-collection mode of the whole diffraction rings, or in translation mode for time-dependent experiments. The apparatus is ideal for collecting medium- to relatively high-resolution diffraction data from diluted or weakly scattering samples and to investigate *in situ* phase changes induced by temperature and/or chemical reactions. The possibility to rapidly collect several good quality diffraction patterns coupled with tunable beam energy allow for multiwavelength experiments such as anomalous XRPD.

Keywords: imaging plate; **in situ diffractometry**; **time-resolved.**

1. Introduction

Imaging-Plate (IP) detectors, combined with high-brilliance synchrotron radiation sources, have proven to yield 2D diffraction data of excellent quality (Garret *et al.*, 1995; Amemiya, 1995; Norby, 1997*a*,*b*) thanks to their relatively good spatial resolution, high linearity and low background noise. Moreover, the possibility to rapidly collect 2D powder diffraction patterns makes these detectors attractive for time-resolved studies in the minute range (Amemiya, 1995; Norby, 1997*a*; Imafuku *et al.*, 1998; Creagh *et al.*, 1998). In a large number of applied fields, like temperature treatment of industrial materials or catalytic reactions, high-quality diffraction data collected in time-resolved mode (TR-XRD) are fundamental for the study of structure transformations induced by temperature or chemical gradients and for the identification of crystalline phases formed during the isothermal or non-isothermal treatments.

The translating imaging-plate technique, successfully employed for time-resolved studies (Imafuku *et al.*, 1998; Creagh *et al.*, 1998; Norby *et al.*, 1999; O'Hare *et al.*, 1998; Norby *et al.*, 1998; Krogh *et al.*, 1998) exploits the experimental principle of the old Guinier–Lenné (Lenné, 1961) and Guinier–Simon (Simon, 1971) cameras: a linear slit selects a narrow portion of the Debye rings while the recording plate linearly translates behind the slits at constant speed allowing to accumulate a continuous diffraction pattern as a function of time. In such a way it is possible to probe the evolution of the sample structure as a function of the time and/or environmental conditions (temperature, pressure, gas atmosphere *etc.*).

The multipurpose IP camera installed on the GILDA (General Italian Line for Diffraction and Absorption) beamline at the European Synchrotron Radiation Facility (ESRF) is described. It represents an upgraded version of the apparatus developed on the X7B beamline at the National Synchrotron Light Source (Brookhaven National Laboratory) (Gualtieri *et al.*, 1996; Norby, 1997*a*). Examples will be provided of the experimental possibilities offered by the apparatus.

2. Technical features

Fig. 1 describes the IP camera set-up installed in the second experimental hutch of the GILDA beamline (Pascarelli *et al.*, 1996; Meneghini *et al.*, 1998). The GILDA focusing optics provide a beam spot of about 2(h) $\times$1(v) mm at the sample position in a wide energy range (8–50 keV). The resolution slit system (vertical and horizontal) (S1) defines the effective spot size with a resolution of $\pm 25\mu$m. The ionization chamber I_o, placed after the S1 slits, monitors the effective photon flux on the sample. The absorber (A) can be inserted to reduce the beam intensity, for example in order to record the direct beam position on the imaging plate or in order to avoid peak saturation. The rotating shutter (SH) regulates the exposure time of the IP. The anti-scattering slit system (S2) and a lead 'nose', placed just before the sample (S) reduce the diffuse background due to air scattering. The beam stopper (BS) prevents the direct beam reaching the imaging plate. Usually powder samples are enclosed in glass or quartz capillaries (with diameters ranging between 0.3 mm and 2 mm) mounted on rotating/oscillating goniometer heads (G) allowing precise alignment of capillary on the rotation axis. Slices or pellets can be mounted as well. A motorized two-axis ('*yz*') translation stage, a red laser beam aligned on the X-ray beam, a microscope and an X-ray CCD camera allow precise and reliable positioning of the sample on the beam. The sample-to-IP distance can be appropriately chosen between about 100 mm to over 400 mm to match experimental requirements (Norby, 1997*a*): larger distances ensure better angular resolution, while shorter distances allow to probe a wider portion of reciprocal space. The instrumental line broadening $\Delta 2\theta$ (FWHM) is mainly determined by (Norby, 1997*a*) the capillary diameter (d_{cap}) and the sample-to-IP distance (D_o),

$$\Delta 2\theta \approx \frac{180}{\pi}\frac{d_{cap}}{D_o}\cos(2\theta) \qquad (1)$$

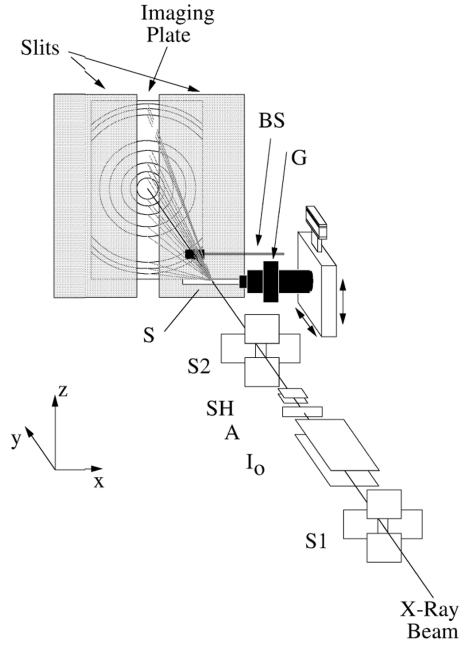

Figure 1
Schematic view of the IP set-up on the GILDA beamline. See text for details.

The instrumental width $\Delta 2\theta < 0.1^\circ$ is typically reached and values down to a few 10^{-2} 2θ Deg. can be obtained on request using thinner capillaries ($d_{cap} = 0.3-0.4$ mm) and larger sample-to-detector distances ($D_o = 300-400$ mm).

The IP camera consists of a magnetic support for the Fuji 200 × 400 mm^2 IP and two 450 mm-high Ta slits. The magnetic support allows easy mounting/removal of the IP with a good reproducibility and minimizes flat plate distortions. The support is mounted on a precision linear translation stage (±350 mm) perpendicular to the incoming X-ray beam. The two slits in front of the IP can be opened from 1 mm to 200 mm; they are mounted on a motor driven translation stage (x) for positioning on the X-ray beam.

The IP camera is aligned perpendicular to the beam through a kinematic base and rotation stage. The base is mounted on a vertical (z) translation stage to adjust the vertical position of the camera (±300 mm) with respect to the beam height.

The latent images stored in the IP are recovered and digitalized using a Fuji BAS2500 laser scanner allowing for a dynamical range of 16 bit/pixel with a minimum pixel size of 50 × 50 μm^2.

The IP camera works in two acquisition modes: full-plate or translating mode. In full-plate mode the slits in front of the IP are completely removed and the whole diffraction pattern is recorded in one shot. This allows to collect high-quality (highest counting statistics) powder diffraction patterns in a short time, ranging from a few tenths of seconds to a few minutes depending on the sample investigated. As an example, Fig. 2 reports an XRD patterns of Y_2O_3 sample collected with the IP camera in 2 min compared with the patterns measured in about 4 h using a scanning diffractometer. In order to compare the statistics of XRD patterns, IP and scanning diffractometers were configured to collect XRD patterns with similar angular resolution ($\Delta 2\theta \approx 0.2^\circ$): the same capillary sample holder ($d_{cap} = 0.7$ mm) was used in both cases and the incoming vertical beam size of 1 mm was selected in order to ensure the complete sample illumination. The sample-to-IP distance was D_o = 155 mm. The diffractometer has been configured in low-resolution mode, *i.e.* using 0.1 mm-resolution slits (instead of a crystal analyzer) on the 2θ goniometer arm at R_g = 200 mm from the sample. In such a configuration the instrumental peak broadening is mainly determined by the goniometer radius R_g, and the sample holder diameter: $\Delta 2\theta \approx (180/\pi)(d_{cap}/R_g)$.

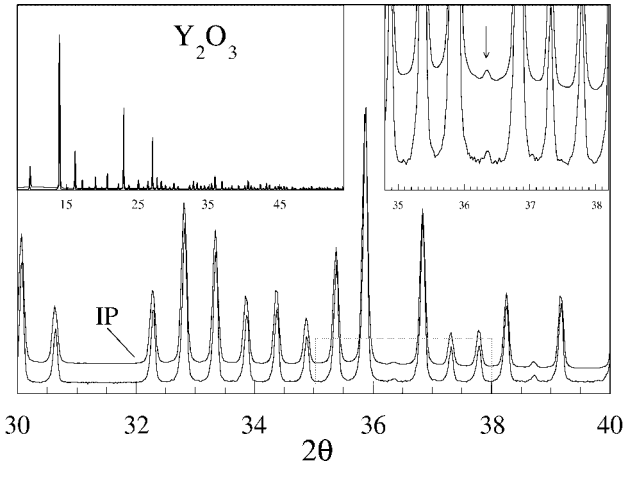

Figure 2
XRD patterns of Y_2O_3 sample collected with the IP camera in about 2 min (upper curves) compared with the pattern collected, on the same sample, using the two-circle diffractometer, in about 4 h (lower curves). Panels highlight different regions of the diffraction patterns.

When working in translating mode the two slits in front of the IP select a vertical slice of the diffraction pattern. The IP moves behind the slits and the diffraction pattern is recorded as a function of time (TR-XRD). The time resolution Δt is a function of the IP camera translation speed v (mm s^{-1}) and slits width S (mm): $\Delta t\,(s) = S/v$. Δt can be widely tuned, in order to match the experimental requirements, between a few seconds and several minutes. This acquisition mode offers several possibilities when applied to the study of dynamical phenomena like the kinetics of temperature-induced phase transition or structural transformations due to chemical reactions.

To perform *in situ* XRD experiments different sample-conditioning devices are available: a gas-flux heater allows to reach 950° C. The real temperature of the sample is evaluated by measuring accurate Rietveld refined lattice parameters of a standard with known thermal expansion coefficient. A reaction chamber (C1) allows to perform *in situ* studies (Norby, 1997*a*,*b*) of the synthesis of microporous materials under hydrothermal conditions. In order to improve the statistical sampling of the powder particles by the incident beam, the design of the reaction chamber allows rotation/oscillation of the sample enclosed in the capillary. Weak pressure (up to 15–20 bar) can be applied using inert gases like N_2.

A reaction chamber (C2) has been designed to be coupled with a mass spectrometer for *in situ* catalyst investigation and is presently being tested (Martorana *et al.*, 2001). It allows to monitor, at the same time, the evolution of the diffraction patterns and the composition of outgoing gases in order to directly relate structural modification of the sample to their chemical activity.

3. Typical applications and results

Area detectors like IPs, CCD cameras and diode arrays offer several advantages with respect to standard single-detector instruments: the exceptional counting statistic and short collection time allow to investigate small sample volume and/or weakly scattering materials and/or highly diluted compounds (as, for example, supported catalysts). On the other hand, collection of a large part of 2D diffraction patterns is particularly suited to work with small sample volume and/or dealing with preferred orientation effects (*e.g.* in high-pressure powder diffraction experiments) since the integration over the Debye–Scherrer rings is the most efficient way to increase the grain statistics and obtain a good averaging. The principal drawbacks of 2D detectors are the angular resolution that is lower than that achievable on high-resolution powder diffraction instruments, and the reduced 2θ range that limits the accessible reciprocal space. It is possible to expand the reciprocal space using tilted IP (Norby, 1997*a*) or cylindrical IP cameras such as those available at the Photon Factory (BIGDIFF) (Creagh *et al.*, 1998), SPring-8 (BL02B2 beamline) (SPring-8, 1998) or at the Synchrotron Radiation Source (9W1 beamline) (Daresbury Laboratory). However, in our opinion, the flat plate geometry allows the larger flexibility, in fact using cylindrical IP cameras the sample-to-detector distance is fixed by the cylinder radius; this reduces the degrees of freedom available to optimize intensity and/or resolution in XRD experiments. Moreover, the instrumental contribution to the FWHM in the flat plate geometry decreases at larger 2θ (eq. 1) providing a better resolution where it is needed the most. The IP detectors present advantages over electronic position-sensitive detectors, in particular when used on high-intensity synchrotron radiation sources: they have better linearity, the line-broadening effect caused by the cross-talk effect between

diodes is reduced as well as the electronic noise. These are substantial advantages when collecting diffractograms on diluted polycrystalline materials in which the relevant information for the phases under investigation are partially masked by the large signal diffused by the supporting media.

The instrumental setting described in this paper is highly suited to perform high-quality powder-diffraction experiments on highly diluted polycrystalline materials and to address TR-XRD experiments as described in the following examples.

3.1. *X-ray powder diffraction and anomalous diffraction on dispersed polycrystalline materials*

Dispersed materials include a large class of materials such as supported catalysts, implanted materials and nanocomposites. In these materials a small amount of 'active phases' are dispersed as small particles (micrometer and nanometer size) into inert matrices. They present peculiar mechanic, optical, electronic and magnetic properties attractive in a number of applied fields. The characterization of these dispersed phases and of their structural modifications induced by preparation methods and/or by successive treatments is fundamental to understand the physical properties of the material, to improve the device performances, and to tailor innovative materials. However, the high dilution of these compounds makes it difficult to use standard powder diffraction techniques since the weak signal of phases under investigation is often masked by the intense background diffused by the support. In this field the performances of an IP detector can be usefully employed to obtain fundamental insights.

We present here example studies performed on supported metallic catalysts. Metallic catalysts are made by small metallic particles dispersed onto inert matrices. Nanometer-sized particles are required to achieve a larger surface-to-volume ratio that improves the reactivity of the catalyst and reduces the amount of precious metal employed. The atomic structure, the particle size distribution, as well their evolution under thermal treatment and/or activity, are relevant information that can be obtained through TR-XRD investigations.

Fig. 3(*a*) reports the diffraction patterns of a carbon-supported Pd catalyst (Pd 0.66 %wt on C) collected in full-plate mode before and after a thermal treatment at 630°C (Canton *et al.*, 2000, 2001). The Bragg peaks relative to the Pd phase are clearly recognized over the C diffuse background. They increase in intensity and become sharper in the annealed sample pointing out the growth of the metal particles. Such a growth of Pd particles is probably related to the ageing processes reducing the activity of catalysts when treated at high temperature. Fig. 3(*b*) reports the values of the Pd lattice parameter a_{Pd}, and Pd particle size D_{Pd}, obtained from the analysis of TR-XRD patterns collected during the sample heating between 25°C and 630°C (heating rate of about 2.5°C/min). The $a_{Pd}(T)$ values evidently depart from the smooth behaviour expected for a thermal expansion effect: $a_{Pd}(T)$ quickly expands upon heating above *ca.* 250°C and it contracts above *ca.* 400°C. This unusual trend indicates the formation of an intermediate $Pd_{1-x}C_x$ ($x \sim 0.1$) solid solution in the temperature range 250–400°C, pointing out a strong interaction between metal and support. At higher temperatures the $Pd_{1-x}C_x$ solution phase dissolves and $a_{Pd}(T)$ recovers the behaviour expected for pure Pd. By looking at the $D_{Pd}(T)$ values it is evident that the Pd particles remain quite small (< 100Å) on heating to about 400°C, then they suddenly start growing. The growth of a metal particle is clearly related to the drop of $a_{Pd}(T)$ and to the dissolution of the $Pd_{1-x}C_x$ phase.

When dealing with dispersed compounds the removal of the intense background scattering diffused from the support is a fundamental step, especially searching for weak effects such as the interactions between the support material and the supported phases or the measurements of very small (nanometer size) particles. Usually this background is taken into account by collecting the diffraction pattern of the pure support in order to subtract it from the data. Nevertheless, the preparation methods and the successive sample treatments can modify the structure of the support itself and the independent measure of the pure support does not ensure a fully reliable procedure.

The anomalous X-ray diffraction (A-XRD) approach represents a more reliable method to separate the structural signal of the embedded phases from that of the support. A-XRD, in fact, takes advantage of the energy dependence of the anomalous dispersion corrections to the atomic scattering factors to give chemically selective structural information. The use of area detectors allows to perform such experiments in a relatively short time, while conventional single-detector instruments would require long (sometimes prohibitively long) acquisition times. Fig. 4 describes a preliminary A-XRD experiment on pumice-supported Pd catalysts (Pd/pumice). Two Pd/pumice samples were prepared with a Pd content of 1.5 %wt (sample *A*) and 0.5 %wt (sample *B*). XRD patterns have been collected in full-plate mode (Fig. 4*b*,*d*) near (–25 eV) and far (–750 eV) from the Pd *K* edge (24350 eV). The collection time was fixed to 10 min for each pattern. The difference patterns $\Delta I = I_{-25} - I_{-750}$, reported in Fig. 4(*a*,*c*), point out the complete removal of the pumice scattering contribution and, also for sample *B*, the Pd structural features become evident. Rietveld structural refinement (Larson & Von Dreele, 1997) of ΔI gave a_{Pd} = 3.8907 (6) for sample *A* and a_{Pd} = 3.892 (2) for sample *B* in good agreement with the Pd bulk. Peak shape analysis indicates larger particles for sample *A* (D_{Pd} = 120 Å) and about three times smaller (D_{Pd} = 40 Å) for sample *B*.

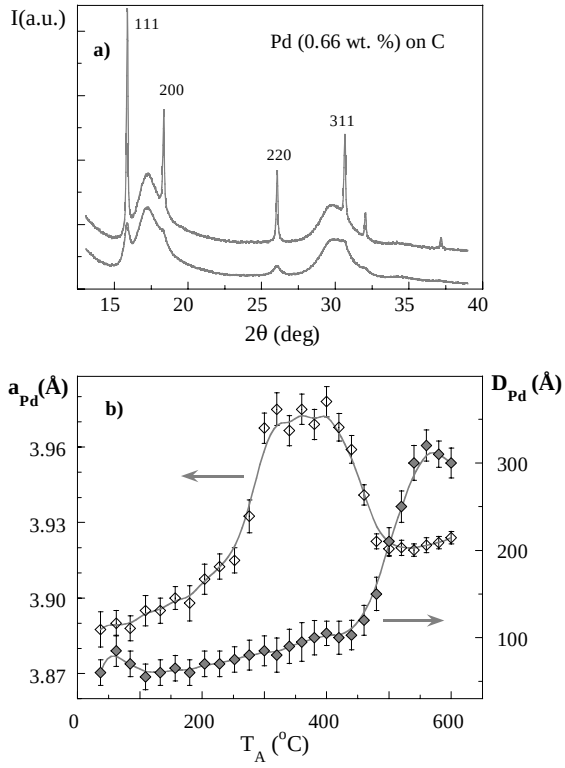

Figure 3
(*a*) XRD on a Pd/C catalyst (x_{Pd} = 0.66 %wt) before (lower curve) and after (upper curve) thermal treatment (shifted for clarity). (*b*) Evolution of the lattice parameter (open diamonds) and grain size (filled diamonds) of the metallic phase during thermal treatment. Lines are guides for the eye.

3.2. Kinetics of crystallization of zeolites

This example describes an experiment on the kinetics of crystallization of zeolites carried out on a system previously tested in laboratory. A clear solution was prepared starting from 3.77 g sodium aluminate, 71.57 g sodium hydroxide, 24.69 g sodium silicate and 280.8 g water, and aged 36 h at room temperature. A 0.7 mm-diameter quartz capillary was filled with the aged solution and kept at a pressure of 8 bar from a nitrogen cylinder during the experiment to obtain hydrothermal conditions in the capillary. The capillary was oscillating ($\pm 60^\circ$) during the experiment to improve statistics and ensure mixing in the crystallizing solution. The temperature was ramped quickly (*ca.* 40°/min) to 110°C and the capillary was kept at that temperature during the isothermal run.

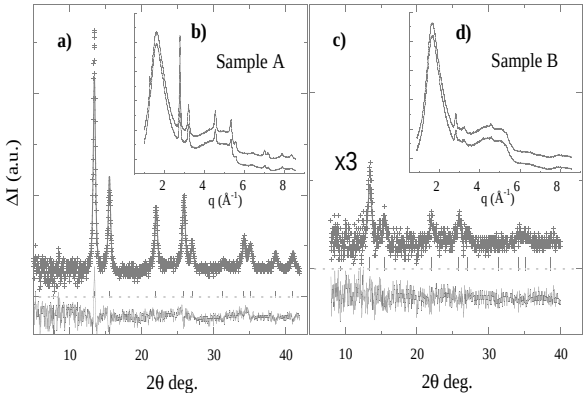

Figure 4
A-XRD on Pd/Pumice catalysts. Full-plate XRD patterns collected at –25 eV (lower curves) and –750 eV (upper curves) below the Pd *K* edge are shown in panels *b* (sample *A*) and *d* (sample *B*) (shifted for clarity). Panels *a* and *c* report difference patterns (crosses) for samples *A* and *B*, respectively. Full lines represent the Rietveld refinement results, markers point out the peak position and, below, the residuals are reported.

Fig. 5(*a*) reports part of the raw image stored on the IP, while Fig. 5(*b*) reports the powder pattern of the final zeolite product formed after the experiment; it was obtained by integration of a slice 3 mm wide along the line '1' in Fig. 5(*a*).

Hydroxysodalite (SOD) is present albeit some residual zeolite Na-A is observed in the pattern (peak positions are marked by stars) which is the precursor of the more stable hydroxysodalite. The crystallization of hydroxysodalite was followed by integrating a 2 mm-wide slice (see for example line '2' in Fig. 5*a*) along the (110), (211), (222), (321) and (330) diffraction peaks of the zeolite diffraction pattern. The raw data (pixels *vs* counts) were converted and renormalized to produce the time *vs* conversion factor (α) plot reported in Fig. 5(*c*). The so-obtained kinetic curve was analyzed using the population balance method (Warzywoda & Thompson, 1989; Katovic *et al.*, 1989*a*,*b*). Assuming an autocatalytic model, it is possible to use a reduced form of the equation described in Warzywoda & Thompson (1989): $\alpha = kt^q$, where k is the rate constant and q is the kinetic order which can be calculated from the plot of $\log(\alpha)$ *vs* $\log(t)$. It gives an indication on the reaction mechanism. In this experiment we obtained q = 2.9 (3) showing that the reaction of crystallization of hydroxysodalite is heterogenous. This suggests that the nucleation of hydroxysodalite takes place on pre-existing crystals of the zeolite Na-A (Ostwald's rule) and not directly from the clear solution.

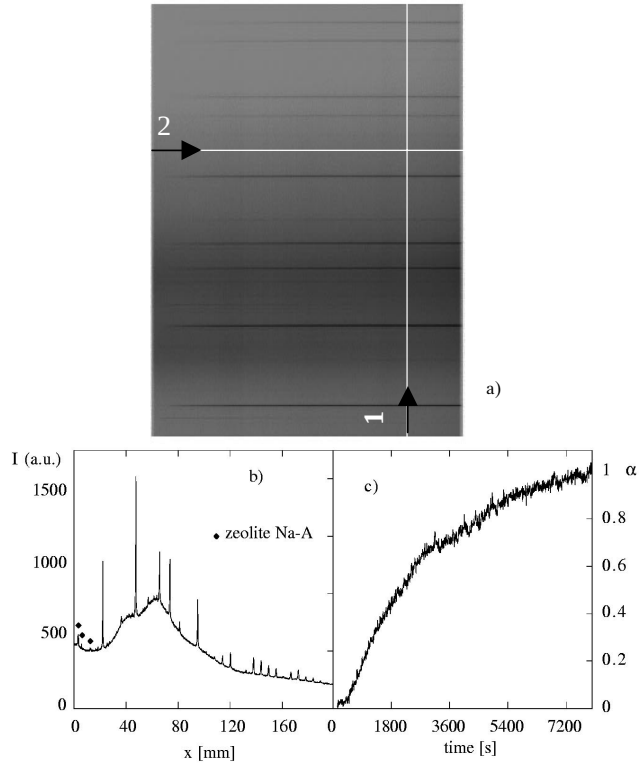

Figure 5
Crystallization of Sodalite at 100°C (see text).

3.3. Transient phases in the hydrothermal synthesis of microporous aluminophosphates

In situ time-resolved synchrotron X-ray powder diffraction was used to follow the hydrothermal synthesis of alkaline earth and transition metal substituted microporous aluminophosphate materials. These materials are of interest in connection with *e.g.* catalysis, and knowledge of crystallization behaviour and the role of templates and chemical composition is important in order to be able to synthesize materials with desired physical and chemical properties. *In situ* powder diffraction is very well suited for kinetic analysis as well as for detection and identification of intermediate (transient) phases. It is well known that templates have a structure-directing effect during synthesis of microporous materials. The present preliminary experiments were performed as part of a study of the structure-directing role of the substituting cations. A series of experiments was performed using a gel composition:

$$(0.4\mathrm{MO} \cdot 0.8\mathrm{Al_2O_3} \cdot \mathrm{P_2O_5}) \cdot x\mathrm{DnPA} \cdot y\mathrm{H_2O}.$$

The template used was di-n-propyl amine (DnPA) and the substituting divalent cations were M = Co^{2+}, Mn^{2+}, Mg^{2+}, Zn^{2+}.

By keeping the gel composition constant, and varying only the type of substituting cation, the effect of the cation on crystallization properties and products can be investigated. *In situ* powder diffraction data were collected with the sample enclosed in 0.7 mm-diameter glass capillaries, as described above. An isothermal mode was used, ramping the temperature quickly (*ca.* 2 min) to 160°C and keeping the temperature for 2 h. Figs. 6(*a*,*b*) show three-dimensional representations of the time-resolved powder diffraction patterns recorded during crystallization of the Co- and Mn-substituted aluminophosphate gels. The end product was in both cases MAPO-11 (with traces of

unidentified phases). In the Mn system, Fig. 6(*a*), a crystalline phase is present initially, but the phase disappears before MnAPO-11 starts crystallizing. A similar initial phase is present in the Mg system, but transforms directly into MgAPO-11. For the Co system, no initial or intermediate crystalline phases are observed, Fig. 6(*b*). In the case of the Zn-substituted aluminophosphate, the starting gel is amorphous, but two intermediate phases are observed prior to the final product. None of the intermediate phases have yet been identified and work is in progress.

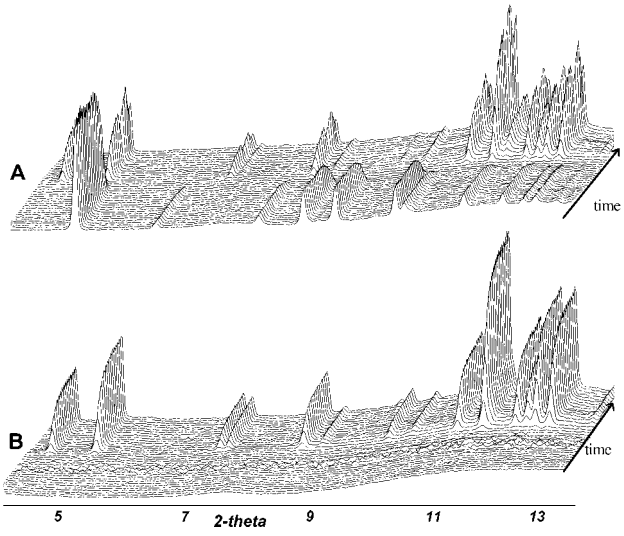

Figure 6
Three-dimensional representations of powder diffraction patterns collected during synthesis of MAPO-11. (*a*) Mn- and (*b*) Co-containing gels.

It is possible that transient layered phases may be formed during hydrothermal synthesis of microporous materials, and identification of these phases is important in determining crystallization mechanisms. *In situ* powder diffraction is a very powerful tool in studying hydrothermal crystallization, as it can be used not only to identify intermediate phases, but can also provide information about transformation kinetics, and data for structure determination and Rietveld refinement of transient phases. The presented initial results will form the basis for the investigations of the structure-directing role of cations, and of the crystallization mechanisms in hydrothermal synthesis of microporous materials.

We thank F. Campolungo, F. D'Anca, V. Sciarra, V. Tullio and P. Venturelli for technical support. The help of Dr C. Dalconi and Dr L. Lusvargi for A-XRD measurements has been greatly appreciated. GILDA is financed by the Italian Institutions CNR, INFM and INFN. The IP camera was partially financed by ASI funds to G. Artioli.

References

Amemiya, Y. (1995). *J. Synchrotron Rad.* **2**, 13–21.
Canton, P., Riello, P., Meneghini, C. & Balerna, A. (2000). GILDA Experiment Report 08–02–193. GILDA, ESRF, Grenoble, France.
Canton, P., Riello, P., Meneghini, C., Balerna, A. & Benedetti, A. (2001). *J. Chem. Phys. B*. In the press.
Creagh, D. C., Foran, G. J., Cookson, D. J., Garret, R. F. & Johnson, F. (1998). *J. Synchrotron Rad.* **5**, 823–825.
Garret, R. F., Cookson, D. J., Foran, G. J., Sabine, T. M., Kennedy, B. J. & Wilkins, S. W. (1995). *Rev. Sci. Instrum.* **66**, 1351–1353.
Gualtieri, A. F., Norby, P., Hanson, J. C. & Hriljac, J.(1996). *J. Appl. Cryst.* **29**, 707–713.
Katovic, A., Subotic, B., Smit, I. & Despotovic, A. (1989*a*). *Zeolites*, **9**, 45–53.
Katovic, A., Subotic, B., Smit, I. & Despotovic, A. (1989*b*). *Zeolites*, **10**, 634–641.
Krogh Andersen, E., Krogh Andersen, I. G., Norby, P. & Hanson, J. C. (1998). *J. Solid State Chem.* **141**, 235–240.
Imafuku, M., Kurosaki, M. & Kawasaki, K. (1998). *J. Synchrotron Rad.* **5**, 935–936.
Larson, A. C. & Von Dreele, R. B. (1997). GSAS General Structure Analysis System. Report LAUR 86–748. Los Alamos National Laboratory, Los Alamos, New Mexico, USA.
Lenné, H. U. (1961). *Z. Kristallogr.* **116**, 190–209.
Martorana, A., Longo, A., Meneghini, C. & Balerna, A. (2001). To be published.
Meneghini, C., Balerna, A., Boscherini, F., Pascarelli, S. & Mobilio, S. (1998). *J. Synchrotron Rad.* **5**, 1258–1262.
Norby, P. (1997*a*). *J. Appl. Cryst.* **30**, 21–30.
Norby, P. (1997*b*). *J. Am. Chem. Soc.* **119**, 5215–5221.
Norby, P., Christensen, A. N. & Hanson, J. C. (1999). *Inorg. Chem.* **38**, 1216–1221.
Norby, P., Poshni, F. I., Grey, C. P., Gualtieri, A. F. & Hanson, J. C. (1998). *J. Phys. Chem. B*, **102**, 839–856.
O'Hare, D., Evans, J. S. O., Francis, R. J., Halasyamani, P. S., Norby, P. & Hanson, J. (1998). *Micropor. Mesopor. Mater.* **21**, 253–262.
Pascarelli, S., Boscherini, F., D'Acapito, F., Hrdy, J., Meneghini, C. & Mobilio, S. (1996). *J. Synchrotron Rad.* **3**, 147–155.
Simon, A. (1971). *J. Appl. Cryst.* **4**, 138–145.
SPring-8 (1998). *SPring-8 Annual Report 1998*. p. 47. SPring-8, Hyogo-ken, Japan.
Warzywoda, J. & Thomson, R. W. (1989). *Zeolites*, **9**, 341–345.